Journal of Zhejiang University-SCIENCE A (Applied Physics & Engineering)
ISSN 1673-565X (Print); ISSN 1862-1775 (Online)
www.jzus.zju.edu.cn; www.springerlink.com
E-mail: jzus@zju.edu.cn

Influence of substrate surface morphology on wetting behavior of tracks during selective laser melting of aluminum-based alloys*

Jie LIU[1,2], Dong-dong GU[†‡1,2], Hong-yu CHEN[1,2], Dong-hua DAI[1,2], Han ZHANG[1,2]
[1]*College of Materials Science and Technology, Nanjing University of Aeronautics and Astronautics, Nanjing 210016, China*
[2]*Jiangsu Provincial Engineering Laboratory for Laser Additive Manufacturing of High-Performance Metallic Components, Nanjing University of Aeronautics and Astronautics, Nanjing 210016, China*
[†]E-mail: dongdonggu@nuaa.edu.cn

Received Nov. 6, 2017; Revision accepted Jan. 10, 2018; Crosschecked Jan. 16, 2018

Abstract: AlSi12 samples were prepared by selective laser melting (SLM) under different processing conditions in order to obtain different top surface morphologies, where single tracks were produced using a fixed processing parameter to reveal the mechanism of the single track on different morphologies. The results show that the morphologies of single tracks changed with roughness of the top surface (Top R_a) of SLM parts, reflected in the variation of wetting angles on the surface processed previously as well as in dimensions of height, width, and depth at the cross-section of each single track. These changes were mainly caused by different wettability and flow behavior of the molten metal under various solidification environments of the single track during SLM. A poor solidification environment in which numerous balls existed limited an effective wetting behavior of molten metal on a previously processed surface of a SLM sample because of an increasing solid-liquid contact area, thus causing dramatical instability of the melt pool and attendant inferior processability of the single track. Meanwhile, under the action of surface tension, the molten metal had a high tendency to transfer into a pore near the single track to form an extending track or flow toward an upper region of melt to form a balling track, hence showing various morphologies of single tracks. This study proposes a theory of the solidification mechanism of single track on the non-ideal surface to provide a better understanding of the SLM processing of Al-Si alloy.

Key words: Selective laser melting (SLM); AlSi12; Surface morphology; Single track
https://doi.org/10.1631/jzus.A1700599 **CLC number:** TN249

1 Introduction

Selective laser melting (SLM), as one of the additive manufacturing (AM) processing methods, is widely used to manufacture 3D parts with complex geometric design and flexible fabrication in a wide variety of metal materials (Zhang and Attar, 2016; Ge et al., 2017). During SLM processing, based on a computer-aided design (CAD) model, a 3D part can be built by layer-wise addition of powder using a laser beam as the energy source (Gu et al., 2012; Shen et al., 2014). It is a promising processing method for melting powder selectively and solidifying rapidly to arbitrary geometry (Averyanova et al., 2012). The thickness of the first layer on the plate which is used as a substrate for the following layer is very small (Yadroitsev et al., 2010) and is determined by the layer thickness of the part. Compared to conventional fabrication technologies, SLM processing is widely applicable in aerospace and biomedical industries because of its ability to produce parts with complex

---

‡ Corresponding author

* Project supported by the National Natural Science Foundation of China (No. 51735005), the National Key Technology Research and Development Program of China (No. 2016YFB1100101), the Key Research and Development Program of Jiangsu Provincial Department of Science and Technology of China (No. BE2016181), and the Priority Academic Program Development of Jiangsu Higher Education Institutions, China

ORCID: Dong-dong GU, https://orcid.org/0000-0002-8258-6935

geometries, its short processing time, and integration of functions (Olakanmi et al., 2015; Körner, 2016).

Aluminum-silicon casting alloys have been widely used in the aerospace and automobile industries owing to low density, good elasticity, high heat conductivity, and excellent corrosion resistance (Kempen et al., 2015; Siddique et al., 2015). However, the drawbacks, including its high reflectivity, sensitivity to hot cracks and porosity and oxide creation, are such that many processing defects can be created in aluminum SLM parts (Louvis et al., 2011). Wang et al. (2014) investigated the effect of atmosphere on the structure and properties of SLM AlSi12 alloy. The results showed that atmosphere had negligible influence on the density or hardness of the parts, while the ductility of the components produced in argon and nitrogen was superior to those fabricated in helium, probably resulting from the formation of pore clusters in the SLM parts. Moreover, Li et al. (2015) reported that AlSi12 with a controllable ultrafine eutectic microstructure and 25% tensile ductility can be obtained by SLM and solution heat treatment. They found that the as-fabricated AlSi12 constituted nano-sized spherical Si particles surrounding a supersaturated Al matrix and the mechanical properties can be tailored by varying the time of subsequent solution heat treatment.

As SLM samples are fabricated by overlap of multiple single tracks, study of the melt pool and morphology of the single track offers useful information required for understanding the solidification mechanism of the single track. Li et al. (2014) systematically studied the effect of different laser powers on formation of single line scans of $Al_{86}Ni_6Y_{4.5}Co_2La_{1.5}$ metallic glass (MG) by SLM. The energy distribution of the fiber laser and the heat transfer affected the morphology, phase transformation, and mechanical properties of the scan tracks. Liu et al. (2018) demonstrated that the difference in cooling rate of the melt pool showed a significant effect on the formation of gradient microstructure and mechanical properties of SLM AlSi10Mg. Compared with the core area of the melt pool with a much lower cooling rate, the surface area was composed of finer Si particles, dendritic structure, and more sub-grains and sub-boundaries, thereby resulting in relatively high hardness and great wear resistance. Yadroitsev et al. (2010) studied the capillary instability of segmental cylinders and the effects of processing parameters on the formation of single tracks in detail. They found that the range of the optimal scan speeds became slightly broad with the increase of laser power and instability of the distortional single tracks occurred at a low scan speed, whereas excessively high speed caused a balling defect. Kempen et al. (2015) investigated a wide range of laser powers and scan speeds to form single tracks of SLM AlSi10Mg to optimize processing parameters and produced fully dense parts with improved mechanical properties. Yadroitsev et al. (2012) found that, in comparison with the factors of laser power and scan speed, layer thickness had less statistical influence on the formation of a single track. Only 8%–9% of the variation of the track width, contact angle, and the remelted depth were caused by the layer thickness. Ge et al. (2017) simulated the melt pool flow patterns and thermal behavior using a computational fluid dynamics (CFD) method and revealed the formation mechanisms of balling defect and distortion of single tracks produced by electron beam melting at constant liner energy. Yadroitsev et al. (2014) studied the geometrical characteristics of the melt pool of a single track of Ti6Al4V in detail. The results showed that the experimental values of widths of melt pools were notably higher in comparison with those calculated by the Carslaw-Jaeger heat conduction equation for a Gaussian heat source in the moving coordinate system. This is mainly caused by the Marangoni flow in the melt pool. Most previous studies paid a lot of attention to the effect of processing parameters (e.g. laser power, scan speed, and layer thickness) on formation of a single track formed on the smooth plate, whereas investigation of surface morphologies of a layer processed previously was lacking.

Due to the presence of rough surface on the powder bed and significant heat accumulation during SLM processing, there is a large difference between spreading and melting behaviors of a single track on the powder bed and on the theoretical surface of substrate. Therefore, in this study, the influence of surface morphologies on wettability and flow of molten metal during the formation of a single track was analyzed, in order to reveal the actual condition of solidification behavior of melting tracks during SLM.

2 Experimental

2.1 Powder material

The chemical composition of AlSi12 used in this study was 87.5% Al, 12.3% Si, 0.15% Fe, and 0.05% Mg (by weight). The morphology of the powder is shown in Fig. 1. The size range of AlSi12 particles was 10–63 μm with an average diameter of 33 μm.

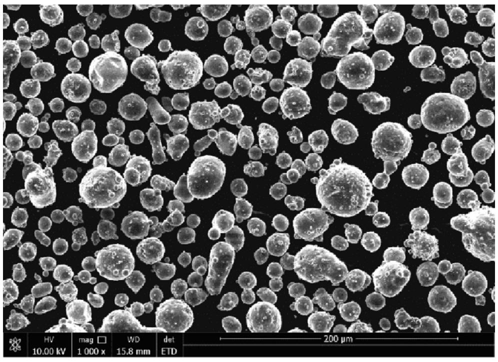

Fig. 1 Morphology of the AlSi12 particles

2.2 Processing and characterization

The SLM machine consists mainly of an YLR-500 ytterbium fiber laser with a maximum power of about 500 W and a spot size of 70 μm (IPG Laser GmbH, Germany), an automatic system for powder delivery, and a computer system for process control. In order to avoid or minimize oxidation, the laser beam works under high vacuum where oxygen content is below 20×10^{-6}.

Specimens with a dimension of 10 mm×10 mm ×5 mm were produced on an aluminum substrate plate. Each layer has a thickness of 30 μm to ensure sufficient overlap among layers. Between the neighboring layers, the orientation rotated by 90°. Hatch spacing was set to 60 μm to ensure sound overlap between tracks. The samples were manufactured using laser powers ranging from 200 W to 400 W in combination with scan speeds in the range of 1000–3000 mm/s during SLM. Each single track was produced at a laser power of 320 W and scan speed of 1000 mm/s on the surface of the sample. The layer thickness of the single track was 50 μm in order to reveal the morphology of the single track. The laser energy per unit length E (J/mm) is denoted by

$$E=P/v, \tag{1}$$

where P is the laser power (W), and v is the scan speed (mm/s).

The as-fabricated samples were cut, ground, and polished according to standard procedures. The images of cross-sectioned single tracks were characterized by PMG3 optical microscope (Olympus Corporation, Japan). The morphologies of the samples and the single tracks were examined by a S-4800 field emission scanning electron microscope (FE-SEM) (Hitachi, Japan) operated at 5 kV. The density was measured by the Archimedes method and surface roughness measurements were conducted using a JB-8c type contact stylus roughness meter (Mitutoyo Company, Japan).

3 Results

3.1 Typical morphologies of single tracks on the samples

Based on relative density and surface roughness, the SLM samples were classified into four regions, as shown in Fig. 2. Fig. 3 gives the corresponding surface morphologies of the samples respectively from the four regions. The sample produced at P of 300 W and v of 1000 mm/s was selected from Region I. A near-fully dense and smooth surface free of balls and pores was obtained and the surface roughness was 5–10 μm (Fig. 3a). For the sample from region II a much higher v of 2000 mm/s was used and a small number of pores and balling particles were formed on

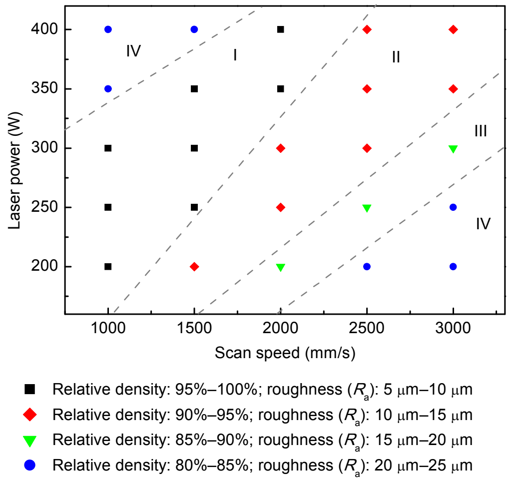

Fig. 2 Distribution of the SLM samples processed by various processing parameters

the surface (Fig. 3b). It is noted that a high v of 3000 mm/s resulted in formation of more pores and splashes in the sample from region III (Fig. 3c) and the roughness of the top surface was about 18.25 μm. As some powder particles were not melted or were in a semi-molten state at a low laser energy, the pores were not completely filled by molten metal, hence leading to poor bonding between the adjacent layers. A combination of high laser power of 350 W and low scan speed of 1000 mm/s resulted in the formation of a large number of balls and splashes, thus increasing the roughness significantly (Fig. 3d).

Fig. 4 shows the characteristic morphologies of the single track formed on the surface with different

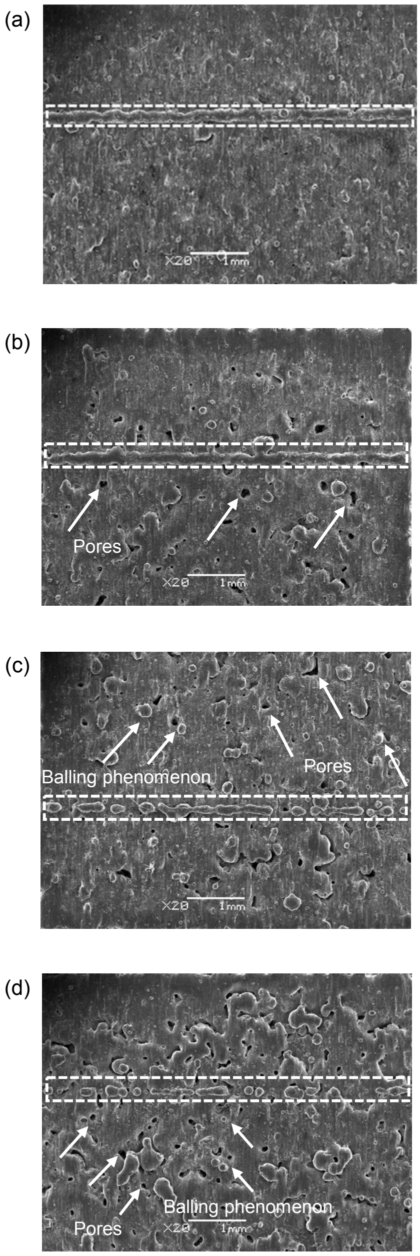

Fig. 3 Surface morphologies of the SLM samples using different processing parameters: (a) dense sample from Region I; (b) sample with less pores from Region II; (c) sample with more pores and balls from Region III; (d) sample with a large number of pores and balls from Region IV

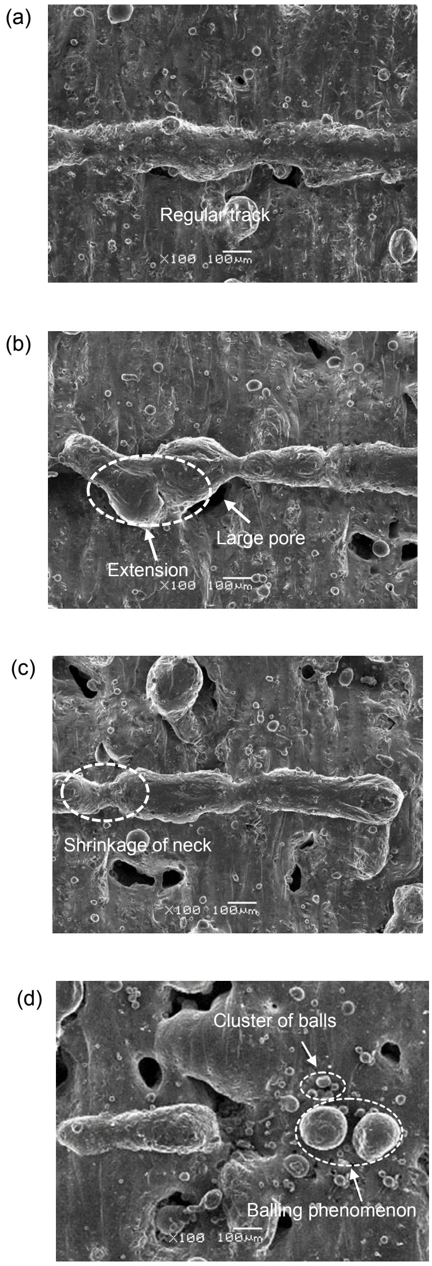

Fig. 4 Four typical types of single tracks prepared on various surface morphologies: (a) regular track; (b) extension of the single track; (c) shrinkage of neck of the single track; (d) balling phenomenon

features. A smooth and flat surface contributes to the formation of a continuous and uniform single track (Fig. 4a). However, an extending track instead of a regular track was observed on the porous surface of the SLM part (Fig. 4b). For the surface with more grooves and splashes, a shrinkage of neck of the single track was observed, as shown in Fig. 4c. This is probably caused by a decreasing amount of molten powder solidifying to a single track on an uneven surface. Balling and break-up of the single tracks occurred when the base surface constituted balling and splashes (Fig. 4d). The numerous metal splashes, balls, and unmelted powder gathering near the single track may reduce the amount of the melted powder of the single track. Although the oxygen content of the ambient gas was less than 0.01% by volume during the SLM processing, the oxides formed on the balls and splashes of AlSi12 showed an unfavorable effect on the wettability of the molten metal.

3.2 Dimensions of cross-section of single tracks

The cross-sections and the corresponding dimensions of the four typical single tracks are shown in Fig. 5 and Fig. 6, respectively. As the morphologies of the single track changed from regular geometry to shrinkage of neck and then to balling, the wetting angles (θ) gradually increased, indicating a decreasing wettability. The dimensions of the cross-sections exhibited a continuous decrease (Fig. 6b). However, the geometrical characteristics of the extending track were very distinctive attaining the smallest wetting angle of the single track and height of the cross-section but the largest width and depth of the melt pool. It is noted that the shape of the melt pool of the single track formed on the smooth and dense sample was regular (Fig. 5a). The wetting angle was about 67°. In this case, the width, remelting depth, and height of the cross-section were measured to be 266.7 μm, 70.1 μm, and 106.3 μm, respectively. For the surface of the sample with large pores, the molten metal flowed in the pore and the single track extended. Sufficient spreading of the molten metal led to relatively large width of the melt pool, so the high magnification of optical microscopy (OM) image cannot fully contain the melt pool. In order to perfectly reveal the dimensions of the melt pool, a lower magnification OM image was used (Fig. 5b). The wetting angle of the extending track reduced to 33°, indicating a significant improvement in the wettability of the single track. The cross-sectional height decreased to 42.8 μm, while the width and depth of the melt pool increased to 321.4 μm and 100.1 μm, respectively. In the case of shrinkage of neck, the wetting angle increased to 82° (Fig. 5c). As the amount of powder was insufficient, a decrease in the width (143.3 μm) and depth (24.3 μm) of the cross-section was observed. For the single track with

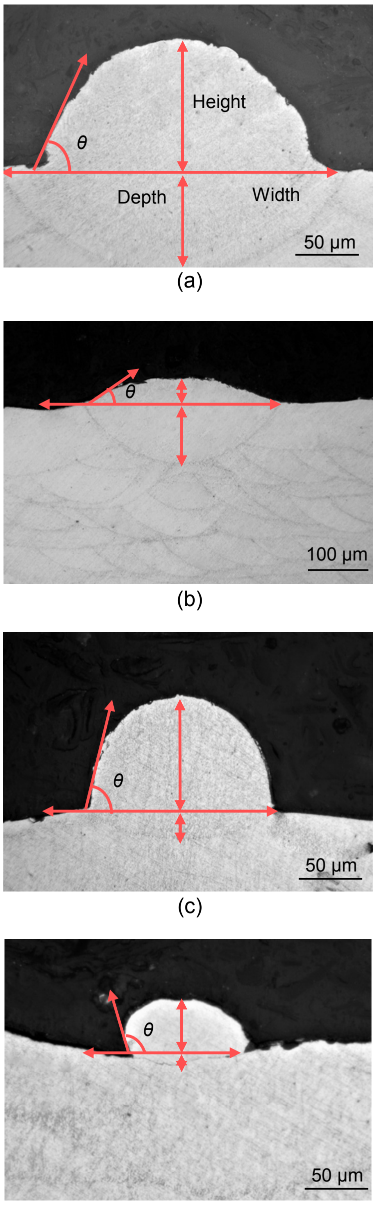

(a)

(b)

(c)

(d)

Fig. 5 Cross-sectioned images of the four typical single tracks: (a) regular type; (b) extending type; (c) shrinkage of neck type; (d) balling type

balling defect (Fig. 5d), the wetting angle reached a value of 108°, revealing a poor wettability of the single track. The remelting region of the single track was much smaller than those of other single tracks (Figs. 5a–5c), which can be deduced from the lower width and depth of the molten pool by 83.3 μm and 10.2 μm, respectively.

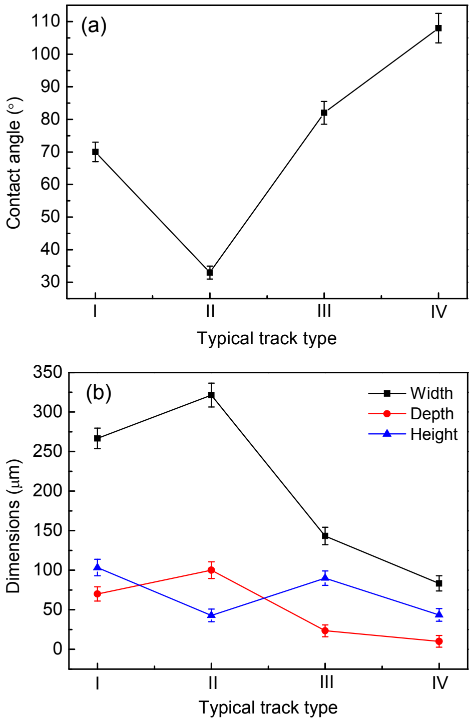

Fig. 6 Measurements of the cross-sections of the four typical single tracks: (a) contact angles on the surface processed previously; (b) dimensions of the cross-sections

4 Discussion

4.1 Effects of surface morphology on wettability

Contact angle θ is a unique characteristic of a solid-liquid-gas system to describe the degree of wetting, which can be expressed by Young's equation as

$$\cos\theta = (\gamma_{\mathrm{SV}} - \gamma_{\mathrm{SL}}) / \gamma_{\mathrm{LV}}, \tag{2}$$

where γ_{SV}, γ_{SL}, and γ_{LV} are the solid-vapor, solid-liquid, and liquid-vapor interfacial tensions. It has to be pointed out that the equation is established on a flat and smooth surface assuming ideal conditions (Fig. 7a).

The contact angle (θ_1) obtained on a rough surface (Fig. 7b) is quite different from that on a smooth and flat surface. Wenzel (1936) introduced the surface roughness coefficient R_{f} (the ratio of the real contact area of solid-liquid to the theoretical contact area):

$$\cos\theta_1 = R_{\mathrm{f}} \cos\theta. \tag{3}$$

The volume of a small drop ignoring gravity (Fig. 7c) is calculated by

$$V = 4\pi R_0^3 / 3, \tag{4}$$

where R_0 is the radius of the drop ignoring gravity.

The fixed volume condition can be expressed by (Ishino et al., 2004)

$$V = \pi R_1^3 (1 - \cos\theta_1)^2 (2 + \cos\theta_1) / 3, \tag{5}$$

where R_1 is the radius of the drop (Fig. 7b).

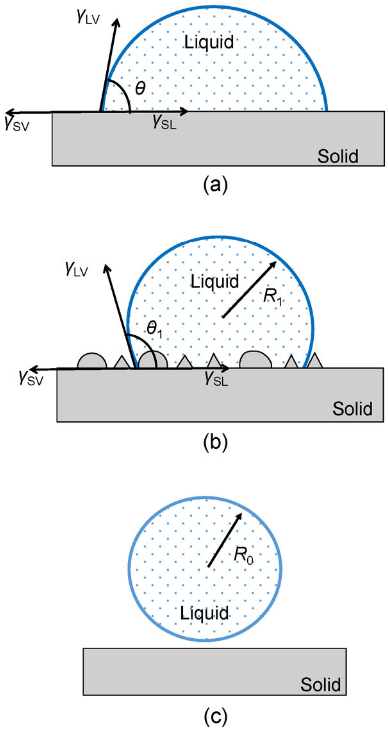

(a)

(b)

(c)

Fig. 7 Contact angle of a liquid on a smooth surface (a), contact angle of a liquid on a coarse surface (b), and a small drop ignoring its gravity (reference state) (c)

The areas of the solid-liquid and liquid-gas interfaces can be estimated by (Ishino et al., 2004)

$$S_{\mathrm{B}}(\theta_1, R_1) = \pi R_1^2 \sin^2 \theta_1, \tag{6}$$

$$S_{\mathrm{C}}(\theta_1, R_1) = 2\pi R_1^2 (1 - \cos \theta_1). \tag{7}$$

The total surface energy at the Wenzel state can be defined by (Ishino et al., 2004)

$$E_{\mathrm{W}} = \gamma_{\mathrm{LV}} S_{\mathrm{C}}(\theta_1, R_1) + (\gamma_{\mathrm{SL}} - \gamma_{\mathrm{SV}}) R_{\mathrm{f}} S_{\mathrm{B}}(\theta_1, R_1). \tag{8}$$

Therefore, the two main factors that affect wettability on a solid surface are surface free energy (E_{W}) and surface roughness. The rough surface actually increases the solid-liquid contact area (S_{B}). As the surface tension of the fluid has a tendency to drive the fluid to reduce its surface area, the fluid droplets reduce their surface area (Eqs. (6) and (7)) by increasing the contact angle (θ_1), resulting in a poor wettability.

The wetting angle (θ_1) can describe the affinity of molten metal to a solid surface, reflecting the ability of spreading of the single track on the processed sample. The wetting of the melt on the surface of the SLM sample involves diffusion, heat transfer with the substrate, and quick solidification at the solid-liquid interface (Das, 2003). Favorable wettability not only improves heat transfer, but also promotes the bonding of the molten metal to the previous layer (Monroy et al., 2015). This has a positive impact on the bonding between interlayers.

The spreading behavior of the liquid droplet follows the famous Tanner law (Gennes, 1985):

$$C_{\mathrm{a}} = \frac{\mu v}{\gamma}, \tag{9}$$

where C_{a} is the number of capillaries, v is the velocity of the liquid flow, γ is the surface tension (Eq. (10)), and μ is the viscosity of the fluid (Eq. (11)). The increase of μ can cause an enhancement of the capillary force exerted on the solid particles by the wetting liquid, which contributes to the rearrangement of particles.

4.2 Formation mechanisms of unfavorable typical tracks

Fig. 8 shows the schematics of formation mechanism of the unfavorable single track on the rough surface of the SLM samples. The large pore on the sample has an important effect on the formation of the single track (Fig. 8a). Since the porous region (i.e. previously solidified region) exhibits a relatively large thermal conductivity compared with the laser irradiated region (i.e. powder region), the quick thermal diffusion of the molten metal in the pore leads to a decrease in temperature (T_1) and attendant high surface tension (γ_1) in comparison with that in the central region of the single track (T_2, γ_2). The surface tension gradient and gravity of melt tend to induce the liquid flow toward the pore. In addition, powder accumulated in the pore tends to be melted, hence increasing the dimensions of the melt pool. Therefore, in this situation, the width and the remelting depth of the melt pool were much larger than those with the other three tracks.

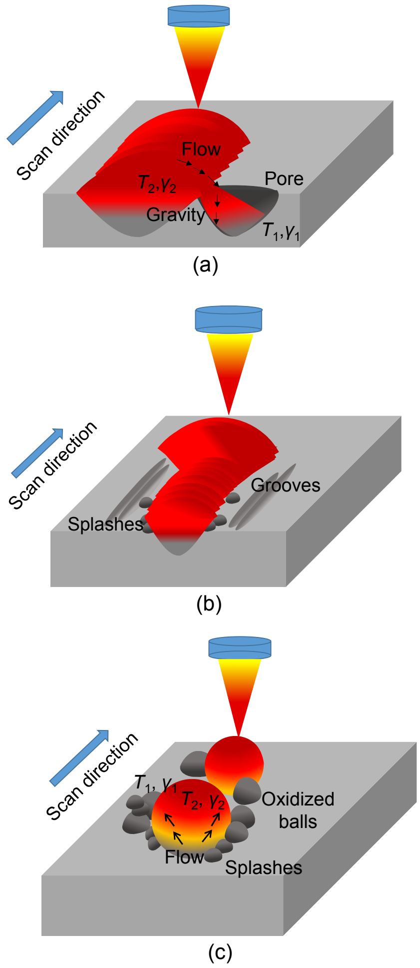

(a)

(b)

(c)

Fig. 8 Schematics of formation mechanism of three typical tracks on the substrates with various surface morphologies: (a) extension; (b) shrinkage of neck; (c) balling phenomenon of the single track

The surface tension γ of the aluminum alloy can be expressed as follows (Gu and Yuan, 2015):

$$\gamma=\left[868-0.152(T-T_{\mathrm{m}})\right]\times10^{-3},\ T>873.2\ \mathrm{K}, \quad (10)$$

where T is the working temperature, and T_{m} is the melting temperature. The surface tension decreases with increase in the working temperature T when T exceeds T_{m}.

The viscosity of the fluid flow can be defined by (Gu and Yuan, 2015)

$$\mu=\frac{16\gamma}{15}\sqrt{\frac{m}{kT}}, \quad (11)$$

where m is the mass of the atom, and k represents the Boltzmann constant.

The flow velocity (v_z) of the molten metal from the hot zone to the cool region can be quantified by the Navier-Stokes equation (Schwarz-Selinger et al., 2001):

$$v_z=\frac{1}{2\mu(T)r}\frac{\partial}{\partial r}rz^2\frac{\partial\gamma(T)}{\partial r}, \quad (12)$$

where z is the melt depth from the surface, and r is the radial coordinates. The origin of the cylindrical coordinate system lies at the center of the sample and the center of the laser beam. A relatively low surface tension (Eq. (10)) at high working temperature leads to a reduced viscosity of the liquid (Eq. (11)) and attendant high flow velocity. It suggests that small viscosity and large gradient of surface tension are essential to improve the flow velocity of molten metal (Eq. (12)).

The flowability can also be estimated from the dimensionless Marangoni number M_{a} (Rombouts et al., 2006):

$$M_{\mathrm{a}}=\frac{\mathrm{d}\gamma_{\mathrm{LV}}}{\mathrm{d}T}\frac{\mathrm{d}T}{\mathrm{d}r}\frac{L}{2\mu\delta}, \quad (13)$$

where $\mathrm{d}T/\mathrm{d}r$ is the temperature gradient, L is the length of the melt pool, and δ is the thermal diffusion coefficient. The high gradient of temperature and attendant increased surface tension gradient lead to an increase of the Marangoni flow intensity.

For a surface with a roughness of 18.25 μm, the grooves and splashes present on the surface cause uneven distribution of the powder on the SLM sample, thus decreasing the amount of powder solidified to single track (Fig. 8b). The melt of the single track combined with the remelted metal of the sample forms the melt pool. It has to be mentioned that penetration in the sample is an additional contribution to the formation of continuous single tracks (Yadroitsev et al., 2010). The amount of the melt wetting the sample is less for lack of molten metal, thus the remelting depth of the sample decreases. This causes instability of the melt pool. Furthermore, the increasing solid-liquid contact area on the rough surface will degrade the wettability. The single track tends to shrink and even splits into several parts to obtain an equilibrium according to the unstable standard, thus forming a discontinuous melting line.

The Plateau-Rayleigh analysis of the instability of the cylindrical liquid indicates that the stability condition of the free liquid column under zero gravity is (Chandrasekhar, 1981):

$$\frac{\pi D}{L}>1, \quad (14)$$

where D is the diameter of the column.

Yadroitsev et al. (2010) gave the stability condition when $\varphi>\pi/2$ (Fig. 9):

$$\frac{\pi D}{L}>2^{1/2}\left[\frac{\varphi(1+\cos(2\varphi))-\sin(2\varphi)}{2\varphi(2+\cos(2\varphi))-3\sin(2\varphi)}\right]^{1/2}, \quad (15)$$

where φ is the angle of the segmental cylinder. The free liquid column is stable at any length when $\varphi<\pi/2$.

The balling phenomenon of the single track on the rough surface with a large number of balls and splashes is also studied (Fig. 8c). For the rough surface, the amount of molten metal for wetting the SLM sample decreases with the reduction of metal powder of the single track. The increase in solid-liquid area due to balls and splashes is responsible for the increasing wetting angle.

It is well known that aluminum has a strong affinity to oxygen. The balls and splashes of aluminum alloy clustering on the surface oxidized very fast even at a very low oxygen level (Louvis et al., 2011). These oxide films have negative effects, e.g. passivating the surface of the molten metal, hindering diffusion, reducing its reaction, and increasing the difficulty of penetrating the surface (Sarou-Kanian et al., 2003). The thin oxide film adhered to the balls forms a smooth surface, and thus reduces the wettability. The poor wetting of the molten metal on the oxide can be explained by the interface energy. The surface free energy of the metal oxide is much lower than that of the corresponding liquid-vapor surface free energy (Das, 2003).

The balling defect can also be caused by Marangoni convection. As the temperature of balls clustering near the single track (T_1) is lower than that of the molten powder in the laser beam (T_2), the thermal diffusion of the upper part of the fluid in contact with the large balls is very fast. The temperature gradient leads to surface tension gradient and attendant Marangoni force (Eq. (13)). The tendency of the fluid flowing upwards results in the limit of wetting of the substrate by the molten metal and eventually in separation of the single line track and the substrate. The liquid metal spontaneously shrinks into a ball to reduce surface energy at the moment when the surface tension is rather high and the melt pool is not in an equilibrium condition (Rombouts et al., 2006).

The minimum time to break up the liquid cylinder can be expressed as follows (Rombouts et al., 2006):

$$t_{\text{break}}=\left\{0.3433\sqrt{\gamma_{\text{LV}}\Big/\left[\rho(D/2)^3\right]}\right\}^{-1}, \tag{16}$$

where ρ is the density of the liquid. The break-up time is proportional to the diameter of the pool. Therefore, a short break-up time is observed when the single track shows balling defects because of the much smaller diameter of the cylinder than those of other single tracks (Fig. 9).

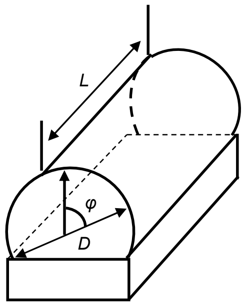

Fig. 9 Segmental cylinder of liquid on the substrate

5 Conclusions

The surface morphologies of the SLM samples processed at various parameters were quite varied. Although the single track was produced at the same processing parameters, the results showed a variety of types of single tracks and sizes of the cross-section formed on different surface morphologies. The main conclusions are as follows:

1. When the single track was formed on the smooth and flat surface of the SLM sample, the powder spread evenly on the surface and the effects of the defects of the sample on the spreading of the powder and the wettability of the molten metal were insignificant. In this situation, there was sufficient molten powder present and the good wettability promoted the formation of a regular single track.

2. In the case of large pores near the single track, there was some powder accumulated in the pore. In addition, the gradients of gravity and the surface tension had a tendency to expel liquid from the pool to the pore, thereby resulting in good wettability. Thus, the single track extended and the width and depth of the melt pool were relatively large.

3. A small amount of molten metal of the single track on the uneven surface was expected to decrease the amount of melt for wetting the SLM sample. A neck shrinking of the single track occurred due to poor wettability of the single track and the instability of the melt pool.

4. The oxide films formed on the balls caused poor wetting on the substrate by molten metal. In addition, the temperature gradient of the molten metal had an influence on the flow direction. As a result, the single track had a tendency to form balls.

References

Averyanova M, Cicala E, Bertrand P, et al., 2012. Experimental design approach to optimize selective laser melting of martensitic 17-4 PH powder: part I–single laser tracks and first layer. *Rapid Prototyping Journal*, 18(1): 28-37.
https://doi.org/10.1108/13552541211193476

Chandrasekhar S, 1981. Hydrodynamic and Hydromagnetic Stability. Dover Publications, New York, USA, p.109-154.

Das S, 2003. Physical aspects of process control in selective laser sintering of metals. *Advanced Engineering Materials*, 5(10):701-711.
https://doi.org/10.1002/adem.200310099

Ge W, Han S, Fang Y, et al., 2017. Mechanism of surface

morphology in electron beam melting of Ti6Al4V based on computational flow patterns. *Applied Surface Science*, 419:150-158.
https://doi.org/10.1016/j.apsusc.2017.05.033

Gennes PGD, 1985. Wetting: statics and dynamics. *Reviews of Modern Physics*, 57(3):827-863.
https://doi.org/10.1103/RevModPhys.57.827

Gu DD, Yuan PP, 2015. Thermal evolution behavior and fluid dynamics during laser additive manufacturing of Al-based nanocomposites: underlying role of reinforcement weight fraction. *Journal of Applied Physics*, 118(23): 233109.
https://doi.org/10.1063/1.4937905

Gu DD, Meiners W, Wissenbach K, et al., 2012. Laser additive manufacturing of metallic components: materials, processes and mechanisms. *International Materials Reviews*, 57(3):133-164.
https://doi.org/10.1179/1743280411Y.0000000014

Ishino C, Okumura K, Quere D, 2004. Wetting transitions on rough surfaces. *Europhysics Letters (EPL)*, 68(3):419-425.
https://doi.org/10.1209/epl/i2004-10206-6

Kempen K, Thijs L, Humbeeck JV, et al., 2015. Processing AlSi10Mg by selective laser melting: parameter optimization and material characterization. *Materials Science & Technology*, 31(8):917-923.
https://doi.org/10.1179/1743284714Y.0000000702

Körner C, 2016. Additive manufacturing of metallic components by selective electron beam melting-a review. *International Materials Reviews*, 61(5):361-377.
https://doi.org/10.1080/09506608.2016.1176289

Li XP, Kang CW, Huang H, et al., 2014. Selective laser melting of an $Al_{86}Ni_6Y_{4.5}Co_2La_{1.5}$, metallic glass: processing, microstructure evolution and mechanical properties. *Materials Science & Engineering: A*, 606(2):370-379.
https://doi.org/10.1016/j.msea.2014.03.097

Li XP, Wang XJ, Saunders M, et al., 2015. A selective laser melting and solution heat treatment refined Al-12Si alloy with a controllable ultrafine eutectic microstructure and 25% tensile ductility. *Acta Materialia*, 95:74-82.
https://doi.org/10.1016/j.actamat.2015.05.017

Liu YJ, Liu Z, Jiang Y, et al., 2018. Gradient in microstructure and mechanical property of selective laser melted AlSi10Mg. *Journal of Alloys and Compounds*, 735: 1414-1421.
https://doi.org/10.1016/j.jallcom.2017.11.020

Louvis E, Fox P, Sutcliffe CJ, 2011. Selective laser melting of aluminium components. *Journal of Materials Processing Technology*, 211(2):275-284.
https://doi.org/10.1016/j.jmatprotec.2010.09.019

Monroy K, Delgado J, Sereno L, et al., 2015. Geometrical feature analysis of Co-Cr-Mo single tracks after selective laser melting processing. *Rapid Prototyping Journal*, 21(3):287-300.
https://doi.org/10.1108/RPJ-11-2013-0122

Olakanmi EO, Cochrane RF, Dalgarno KW, 2015. A review on selective laser sintering/melting (SLS/SLM) of aluminium alloy powders: processing, microstructure, and properties. *Progress in Materials Science*, 74:401-477.
https://doi.org/10.1016/j.pmatsci.2015.03.002

Rombouts M, Kruth JP, Froyen L, et al., 2006. Fundamentals of selective laser melting of alloyed steel powders. 56th General Assembly of CIRP, p.187-192.

Sarou-Kanian V, Millot F, Rifflet JC, 2003. Surface tension and density of oxygen-free liquid aluminum at high temperature. *International Journal of Thermophysics*, 24(1):277-286.
https://doi.org/10.1023/A:1022466319501

Schwarz-Selinger T, Cahill DG, Chen SC, et al., 2001. Micron-scale modifications of Si, surface morphology by pulsed-laser texturing. *Physical Review B*, 64(15): 155323.
https://doi.org/10.1103/PhysRevB.64.155323

Shen YO, Cantwell W, Li Y, 2014. Skin-core adhesion in high performance sandwich structures. *Journal of Zhejiang University-SCIENCE A (Applied Physics & Engineering)*, 15(1):61-67.
https://doi.org/10.1631/jzus.A1300283

Siddique S, Imran M, Wycisk E, et al., 2015. Influence of process-induced microstructure and imperfections on mechanical properties of AlSi12 processed by selective laser melting. *Journal of Materials Processing Technology*, 221:205-213.
https://doi.org/10.1016/j.jmatprotec.2015.02.023

Wang XJ, Zhang LC, Fang MH, et al., 2014. The effect of atmosphere on the structure and properties of a selective laser melted Al-12Si alloy. *Materials Science & Engineering: A*, 597:370-375.
https://doi.org/10.1016/j.msea.2014.01.012

Wenzel RN, 1936. Resistance of solid surfaces to wetting by water. *Industrial & Engineering Chemistry*, 28(8):988-994.
https://doi.org/10.1021/ie50320a024

Yadroitsev I, Gusarov A, Yadroitsava I, et al., 2010. Single track formation in selective laser melting of metal powders. *Journal of Materials Processing Technology*, 210(12):1624-1631.
https://doi.org/10.1016/j.jmatprotec.2010.05.010

Yadroitsev I, Yadroitsava I, Smurov I, et al., 2012. Factor analysis of selective laser melting process parameters and geometrical characteristics of synthesized single tracks. *Rapid Prototyping Journal*, 18(3):201-208.
https://doi.org/10.1108/13552541211218117

Yadroitsev I, Krakhmalev P, Yadroitsava I, 2014. Selective laser melting of Ti6Al4V alloy for biomedical applications: temperature monitoring and microstructural evolution. *Journal of Alloys & Compounds*, 583(2):404-409.
https://doi.org/10.1016/j.jallcom.2013.08.183

Zhang L, Attar H, 2016. Selective laser melting of titanium alloys and titanium matrix composites for biomedical applications: a review. *Advanced Engineering Materials*, 18(4):463-475.
https://doi.org/10.1002/adem.201500419

中文概要

题　目：选区激光熔化铝合金基底表面形貌对轨道润湿行为的影响

目　的：研究选区激光熔化（SLM）过程中形貌差异较大的块体表面单道成形工艺性，分析单道的润湿行为，为进一步揭示 SLM 加工过程中熔化轨迹的凝固行为提供理论基础。

创新点：1. 系统研究在不同加工参数下形成的不同表面形貌的块体上加工同一参数的单道；2. 基于熔体流动理论，分析在 SLM 加工过程中已加工层存在的大量的热积累以及粗糙的成形表面对单道的润湿行为的影响。

方　法：1. 对在不同形貌的块体上形成的单道进行分析，将单道形貌分为 4 种典型类型（图 4）。2. 通过分析单道横截面的几何尺寸（图 5 和 6），研究表面形貌对单道成形工艺性的影响。3. 基于 Wenzel 方程（公式（3））分析熔体在粗糙表面的润湿行为并基于 Navier-Stokes 方程（公式（12））和 Marangoni 方程（公式（13））分析熔体流动行为。

结　论：1. 块体表面光滑、平整时，粉末在表面铺展均匀、熔化充分、润湿性好，有利于形成连续、规则的单道。2. 单道附近的块体表面存在较大孔隙时，孔隙中会积累一定量的粉末。熔融金属的重力和表面张力共同驱使液体向孔隙流动，单道出现扩展效应：润湿角明显减小，熔池宽度和深度增加。3. 块体表面球化颗粒及飞溅物增多时，表面凹凸不平，单道处熔化的粉末量减少，对基板的润湿性较差，熔池不稳定，导致单道出现颈缩。4. 块体表面存在大量球化颗粒和飞溅物时，单道附近团聚的铝合金球化颗粒极易被氧化，氧化膜使得颗粒表面光滑，从而难以被熔融金属润湿。此外，熔融金属的较大的温度梯度对熔体流动方向也有显著影响，易诱导单道出现球化效应。

关键词：选区激光熔化（SLM）；AlSi12；表面形貌；单道